Effect of the Volume Energy Density and Heat Treatment on the Defect, Microstructure, and Hardness of L-PBF Inconel 625

H.R. JAVIDRAD and SINA SALEMI

In this article, we investigated the effect of the process parameters and heat treatment on the defect formation, microstructure, and hardness of Inconel 625 manufactured by the laser powder-bed fusion (L-PBF) process. Specimens were fabricated with various scan speeds, laser powers, and hatch spacing to give a range of volume energy density (VED) between 108 and 156 J/mm^3. SEM analysis was conducted to identify the effects of the VED on the various defects. A columnar-dendritic microstructure was found in all specimens. The effect of heat treatment on the microstructure, including grain growth, carbide precipitations, and phase transformation, was also studied. The results of this study show that VED has an influential effect on the formation of defects, such as lack of fusion porosity, keyhole, gas pores, and micro-cracks. The microstructure and hardness dependency of the L-PBF Inconel 625 material on the VED and heat treatment emphasizes the importance of the optimum selection of VED and post-processing in the L-PBF manufacturing procedure. Finally, the hardness of the heat-treated and as-built specimens was measured, and their variations with VED were specified.

I. INTRODUCTION

ADDITIVE manufacturing (AM) is a rapidly growing industry that enables the production of complex and lightweight products without requiring any tooling.[1,2] The laser powder bed fusion (L-PBF) process is one of the most common AM methods in which the near-net-shape product is built layer by layer using the powder material from a CAD model.[3] With the recent advancements in AM-based processes, several alloys have been developed to make the fabrication of high-value components through AM processes feasible. Among them, nickel-based superalloys have gained more attention because of their high price and special applications in high-temperature conditions such as gas turbines.[4,5] Inconel 625 (IN625) is a weldable nickel-based superalloy that is well known for its excellent corrosion and fatigue resistance.[6] The high strength of IN625 is due to the solid-solution hardening effect of niobium (Nb) and molybdenum (Mo) that exists within the Ni-Cr matrix.[7] Casting and forging are the most popular methods for the fabrication of parts of nickel-based superalloys[8]; however, the conventional manufacturing processes require complex tooling, and controlling the quality and performance of the products is also challenging. Thus, AM technology, with its novel facilities, has become attractive for the fabrication of these superalloys.[9]

Although AM methods have resolved many of the problems encountered in conventional manufacturing of nickel-based superalloy products, new problems such as fabricating fully dense products, dealing with non-equilibrium phase formation, and achieving desirable mechanical properties have arisen.[10,11] In fact, several factors contribute to the mass density rate and mechanical properties of the final product, making precise adjustment and design of the manufacturing process very challenging.[12] To identify the impacts of the process parameters on the mechanical properties and mass density of the AM products, many research works have been conducted in the research community.[13–19]

Gonzalez et al.[4] carried out a comparative study on the powder bed AM methods of fabricating IN625. They specified that the L-PBF is the only AM method with the capability of producing near-wrought material properties. Amirjan et al.[15] studied the effect of scanning strategy on the quality and mechanical properties of the selective laser melted (SLM) Inconel 718 specimens. Their results depicted that by increasing the scan speed in any given scan strategy, the mass density decreased. They also added that the island scanning

H.R. JAVIDRAD is with the Department of Mechanical Engineering, Iran University of Science and Technology, Tehran 16557, Iran. Contact e-mail: h_javidrad@alumni.iust.ac.ir SINA SALEMI is with the Division of Mechanical Engineering, Niroo Research Institute, Tehran 14686, Iran.

strategy with a 90-deg interlayer rotation yields the highest mass density (*i.e.*, 8.20 g/cm^3). Sateesh *et al.*[13] found that an increase in the scan speed and hatch spacing can increase the micro-hardness but decrease the mass density because of the lack of fusion of IN625 powder particles. Anam *et al.*[18] analyzed SLMed IN625 specimens with a constant VED and obtained a mass density higher than that of the wrought material. The highest value they reached was 8.48 g/cm^3 through a laser power of 195 W, layer thickness of 20 μm, scan speed of 800 mm/s, and hatch spacing of 0.1 mm. Koutiri *et al.*[16] manufactured IN625 specimens with various process parameters to investigate the effect of the process variables on the porosity, surface roughness, and fatigue behavior of the product. They found that when different laser beam diameters were used, the energy density does not fully address the correlation between the process parameters and specimen properties. Criales *et al.*[17] conducted a comprehensive study to identify the impact of process parameters on the melt pool dimension and mass density of L-PBF IN625. They pointed out that the melt pool size and shape change dynamically along a scan track that provides us deeper knowledge about the L-PBF process and defect formation. Moussaoui *et al.*[19] found that by increasing the VED from 30 to 60 J/mm^3, the porosity rate of the specimens decreased from 1.5 to 0.4 pct.

Regarding the microstructural evaluation of L-PBFed IN625 specimens, there are numerous reports in the literature that point to the existence of a fine dendritic microstructure caused by the high cooling rates ($\sim 10^4$ to 10^6 K/s) (*e.g.*, Reference 20). Li *et al.*[8] found that the dendritic arm spacing (DAS) is approximately 0.5 μm when rapid cooling takes place. Zubak *et al.*[21] showed that the powder composition has a significant effect on the microstructure and contributing phases of the direct energy deposition (DED) and L-PBF of IN625. They found that the fraction of Fe, Ti, and Si elements has the highest impact on the formation of the Laves phase. According to their findings, high Fe ($\sim$ 4 wt pct) and high Si (0.05 wt pct) lead to the formation of the Laves phase, and a high amount of Ti (0.19 wt pct) results in the formation of nitrides rich in Ti. Furthermore, it was shown that the presence of the C element increases the tendency to NbC formation, which can prevent the formation of Laves phase.[22] Foster *et al.*[23] investigated the correlation among the process, defect, properties, and structure in L-PBFed Inconel 718. They built several specimens with fixed 200W laser power and different exposure times (80 to 110 μs) and point spacing (80 to 110 μm). They found that by increasing the scan speed for fixed laser power and spot size, the porosity percentage increased with a steep slope.

It is obvious that the final microstructure has a major impact on the mechanical properties. The as-built columnar microstructure may not be proper for all applications because of its high hardness, high tensile residual stress, low toughness, and anisotropic characteristics.[8,19] As stated in the literature, as-built IN625 made by AM processes retains some mechanical properties that differ from the properties obtained by forging or casting.[10] Thus, an appropriate post-processing

strategy is required to obtain a specific and homogeneous microstructure as well as to minimize the residual stress.[20,24,25] Currently, several heat treatment procedures are employed for the nickel-based components, including stress relief, recrystallization, solution annealing, aging, and hot isostatic pressing (HIP) with different combinations and durations.[20] Raghavan *et al.*[25] employed various heat treatments and studied their effects on the microstructure and mechanical properties of the Inconel 718. They found that recrystallization occurred after heat treatment, however, grains remained columnar. They also showed that due to hardening precipitates after the aging process, tensile strength significantly improved. Popovich *et al.*[5] kept SLMed Inconel 718 at 850 °C for 2 hour and found that the porosity rate increased compared with the as-processed state. This may be affected by stress relaxation and cracks during heat treatment. Marchese *et al.*[26] carried out various heat treatment processes on IN625 to investigate the effects of heat treatment on the hardness, microstructure, and mechanical properties. Their work showed that solutioning treatment at 1150 °C for 2 hour followed by aging at 700 °C for 24 hour causes recrystallization and generation of γ'' as well as $M_{23}C_6$ carbides. Li *et al.*[10] employed different heat treatments to minimize residual stresses and to study the microstructural evolution of IN625 specimens. They concluded that, after heat treatment, the grain size increased, a high value of MC precipitates was observed, and grain dislocation was reduced. Lass *et al.*[27] found that the dissolution of δ and γ'' phases takes place after 15 minutes annealing at the temperature of 1150 °C. Many studies have showed that annealing treatment reduces the hardness of the nickel-based alloys. For instance, Hassanin *et al.*[28] observed 25 pct hardness reduction after the first 30 minutes of heat treatment at 1100 °C. All in all, until now, no optimum heat treatment process has been suggested for nickel-based superalloys.

The aim of this study is twofold. First, the microstructural and defect characteristics of IN625 specimens that were manufactured by the L-PBF process are investigated. Second, the phase evolution and hardness variation of IN625 specimens during the heat treatment process are studied. To this goal, we carried out experiments to address the effect of process parameters on the mass density and defect formation of the specimens. Then, we studied the microstructural characteristics of the specimens in both as-built and heat-treated conditions. Finally, hardness measurements were carried out, and the effect of contributing phases on hardness was discussed.

II. MATERIALS AND METHODS

A. *Specimen Preparation*

For a chain of experiments, eight cubic specimens (30 × 30 × 30 mm^3) were fabricated with different process parameters using the EOSINT M250 Xtended L-PBF machine in an argon-filled atmosphere. In the

manufacturing process, a 200W Yb-fiber laser and 100 μm focus beam diameter were used. The laser wavelength was 1060 nm and focus diameter was between 150 and 350 μm. The composition of the IN625 powder, supplied by EOS Company and in accordance with the UNS N06625 standard, is given in Table 1. The layer thickness was 20 μm with a soft-brush coater setting. The laser power, scan speed, and hatch spacing were the process parameters altered in each specimen preparation. It is assumed that the combined effects of the process parameters can be summarized in the VED. The process parameters were designed in a way that covers the VED range of 108 to 156 J/mm^3. Table II presents the adopted process parameters together with the resulting VED as determined using Eq. [1].

$$\text{VED} = \frac{P}{v \cdot t \cdot h} \qquad [1]$$

where P (W) is the laser power, v (mm/s) is the laser scan speed, and, t (mm) and h (mm) denote the layer thickness and hatch spacing, respectively. The line scan strategy with 0/90 degree build angle rotation was applied as shown in Figure 1. The "all core" build pattern was also implemented, in which all the surfaces and the core of the specimens were built with an identical strategy. During the fabrication process, the temperature of the building platform was kept constant at 80 °C, and after the fabrication procedure, no initial stress-relief heat treatment was applied.

For the purpose of this study, each specimen was cut from the middle section of the built specimens by wire EDM to eliminate the effect of near-surface defects on the microstructural analysis. After the desired analysis of the as-built specimens, heat treatment was applied. The heat treatment process includes 1 hour solution annealing at 1100 °C followed by 8 hour aging at 700 °C and air cooling between stages. Aging duration and holding temperature were selected by considering the time-temperature-transformation (T-T-T) diagram of IN625[30] in a way to avoid formation of Laves and δ phases. Before analyzing, all specimens were ground, polished, and etched by a solution composed of 20 mL HCl, 20 mL H_2O, and 4 g $CuSo_4$ for 20 seconds.

Table I. IN625 Powder Composition.[29]

Element	Wt Pct
Ni	58
Cr	20.00 to 23.00
Mo	8.00 to 10.00
Nb	3.15 to 4.15
Fe	5
Ti	0.4
Al	0.4
Co	1
C	0.1
Ta	0.05
Si	0.5
Mn	0.5

B. *Experimental Procedure*

The microstructural characteristics of all specimens, including mass density and porosity measurements, hardness, and phase evolution were analyzed and compared with the heat-treated condition. Microstructural studies were carried out using a scanning electron microscope (SEM) coupled with an energy dispersion spectrum (EDS) detecting system. ImageJ software was utilized for in-frame measurements and analysis. For density measurements, the Archimedes' method was used utilizing a $\pm$ 0.0001 g weighing machine. Every measurement was repeated three times per uncut specimen according to the ASTM B962 standard. Vickers macro-hardness tests (HV30) with a 20-seconds load duration were carried out according to the ASTM E92 standard on the top (*i.e.*, perpendicular to the build direction) and side surface (*i.e.*, parallel to the build direction) of each polished specimen in both as-built and heat-treated states. The macro-scale hardness test was chosen because of its higher reliability in the determination of hardness in specimens with different porosity rates and precipitates. However, to increase the accuracy of the hardness measurement, each test was repeated five times per surface and the average value was determined.

III. RESULTS AND DISCUSSIONS

A. *Density Measurements*

Figure 2 represents the resulting mass density versus VED, adapting from the authors' previous study.[31] It is seen that the mass density increased sharply to around 8440 kg/m^3 at 122 J/mm^3 and then reached a plateau. The reason for the low mass densities in low VEDs can be attributed to the porosity formation resulting from insufficient input energy and lack of fusion. Criales et al.[17] obtained nearly the same mass density for a specimen fabricated by a set of process parameters similar to our S3 specimen. Furthermore, Anam et al.[18] reported the average mass density of 8424 kg/m^3 for the same process parameters as for specimen S5 with a mass density of 8421 kg/m^3. As Figure 2 shows, almost no defect exists in the SEM image from the top surface of the S8 specimen. By comparing the resulting mass density of S4 and S5, it could be seen that although the VED of both specimens was similar, the S5 specimen had higher mass density. Thus, the effect of scan speed is

Table II. Process Parameter Configuration

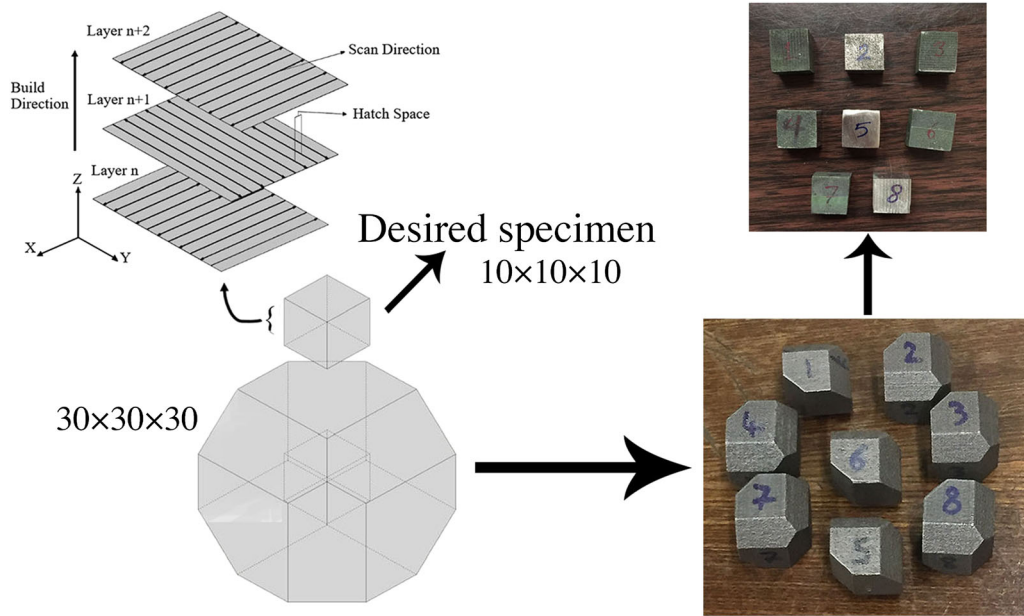| Specimen No.	P (W)	h (μm)	v (mm/s)	VED (J/mm^3)
S1	156	80	900	108.3
S2	150	90	750	111.1
S3	169	90	800	117.4
S4	195	90	900	120.4
S5	195	100	800	121.9
S6	182	90	725	139.5
S7	195	80	800	152.3
S8	175	80	700	156.2

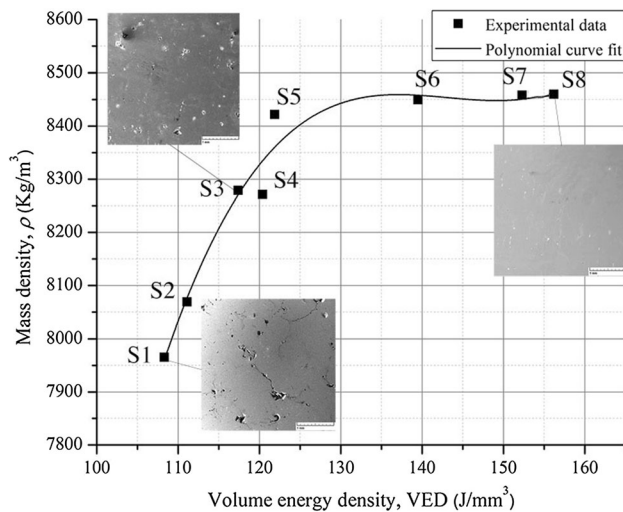Fig. 1—Schematic of the scan strategy in the L-PBF process.

Fig. 2—Relationship between the achieved mass density and VED Adapted with permission from Ref. [31].

more critical than that of hatch spacing. Considering the mass density of specimens S3 and S4, it can be stated that with a constant hatch spacing, by increasing the laser power to some extent, we can increase the scan speed, which assists in achieving a higher production rate. Specimen S2 was built through an exact set of parameters (*i.e.*, layer thickness, laser power, scan speed, and hatch spacing) adapted from another study[32]; however, the resulting density defers a lot. Pleass and Jothi[32] used an island scan strategy coupled with the down- and up-skin technique and obtained a relative density of 99.95 pct. This proves the significance of using a proper scan strategy compatible with the designed VED.

B. Defect Characterization

General anomalies in the L-PBF products can be classified into four different types: (1) lack of fusion (LoF) porosity, (2) keyhole defect, (3) gas pores, and (4) micro-cracks.

Regarding the different melting points of the contributing elements in the powder material, when the input energy was insufficient, the powder particles were partially melted and trapped during the manufacturing process, making LoF defects. Furthermore, low input energy can cause balling defects during the scanning of a particular layer. This excessive surface roughness causes defects during the spreading and melting of the next layers.[33] Another cause of LoF defects could be the uneven powder particle height, which causes cavities filled with unmelted powder.[10] The LoF anomaly is commonly considered a severe defect and can lead to a drastic reduction in mechanical properties.[34] Figure 3(a) shows a LoF defect detected within specimen S1, which is fabricated with the lowest VED in this study. Partially melted particles and lack of fusion are clearly observable. It is worth pointing out that LoF was almost eliminated in the high VED specimens (*e.g.*, S7 and S8).

In the case of excessive input energy, the elements with low melting points evaporate and are trapped under a thin solidified layer that collapses during the scanning of the next layer to form an irregular keyhole-like defect. A keyhole defect similar to LoF is a severe anomaly and must be prevented in manufacturing processes. Figure 3(b), which is taken from specimen S7, shows the keyhole defects that elongated through several layers of the as-built material.

Gas pores are spherical defects that may occur when air, moisture, or the inert gas (*e.g.*, argon or nitrogen) is entrapped within the raw powder material during the
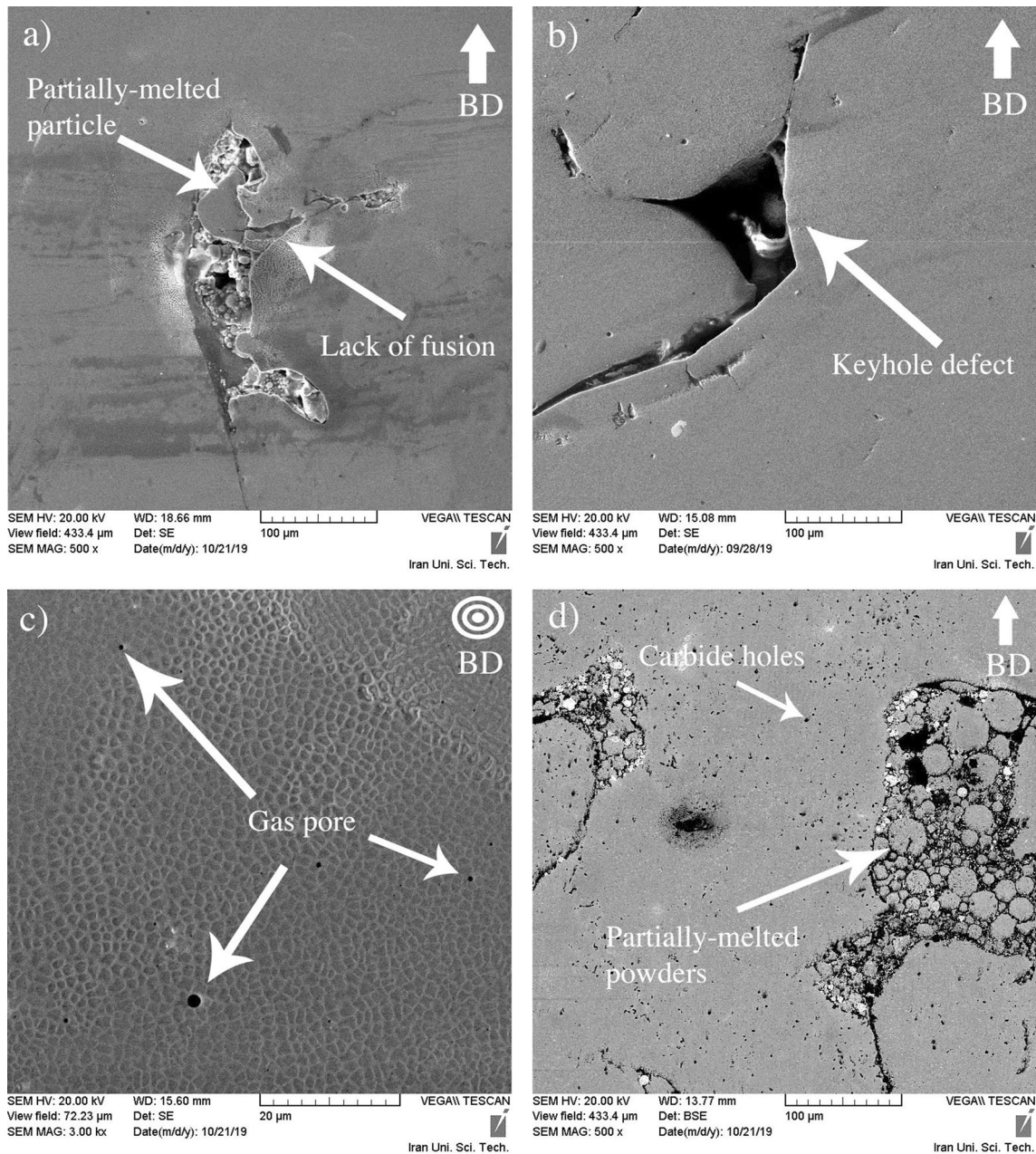
Fig. 3—(*a*) A LoF defect detected within specimen S1; (*b*) a keyhole defect from specimen S7; (*c*) gas pores from specimen S5; (*d*) partially melted powders on the top surface of the heat-treated S1 specimen (BD denotes the build direction).

melting process.[34] The exact sources of this type of porosity are still under discussion, but there is no trusted strategy to eliminate it.[34] We detected gas pores in all of our specimens; however, their populations and sizes were different and seemed to be related to the VED. The population of gas pores increased from S1 to S8 while their diameter decreased. Most of the pores have submicron diameters, although pores as large as 2 μm have also been detected. By observing the SEM images of the top surface of the as-built specimens, most gas pores were concentrated within the inter-dendritic regions. Figure 3(c) shows the top surface of the S5 specimen, where the arrows indicate some of the existing gas pores.

It is believed that heat treatment alone has no significant effect on defect exclusion.[35] Thus, concerning the melting point of IN625 (~ 1300 °C),[4] we cannot expect the elimination of LoF defects by the heat treatment. Figure 3(d) shows the partially melted powders on the top surface of the heat-treated S1 specimen, which resulted from insufficient energy input during fabrication. The dark spots are the cavities that resulted from removing the carbide precipitates during the etching process. By measurement, the diameter of unfused powder particles was estimated to be between 5 and 40 μm (Figure 3(d)).

Another common defect during the L-PBF process of nickel-based alloys is the micro-cracks that arise mainly because of shrinkage of the rapidly solidified material and the subsequent residual stress. Crack elimination in nickel-based alloys is a challenging task and requires using the optimum parameters throughout the manufacturing process.[36] Although micro-cracks are not specific to low-density materials and can also be seen in high-density specimens,[37] it is confirmed that high VED specimens (*i.e.*, S7 and S8) are less susceptible to cracking occurrence. In general, solidification cracking (SC), liquation cracking, ductility-dip cracking (DDC), and post-weld heat treat (PWHT) or strain-age (reheat) cracking (SAC) are the four mechanisms that induce cracks in AM-processed nickel-based alloys.[33]

The SC mechanism contributes to the high cooling rate and segregation of elements within grain boundaries. Liquation cracking occurs because of the formation of a liquid film within the bulk material when it is heated to some extent.[36] DDC is a solid-phase cracking mechanism that mostly occurs at 0.5 to 0.7 of the alloy's melting point in the grain boundaries.[36] Marchese *et al.*[37] stated that the precipitation of carbides in the grain boundaries and residual stress concentration cause material brittleness and crack initiation within the nickel-based materials. PWHT or SAC occurs mainly because of reheating as a result of layer-by-layer manufacturing or improper heat treatment. Figure 4 depicts an example of an inter-granular SC that occurred at the top surface of the S4 specimen with > 150 μm length. As Figure 4 shows, cracks propagated through the inter-dendritic region, which is known to contain high concentrations of Nb and Mo atoms. Due to the high concentration of C atoms within the raw material, brittle MC carbides are expected to form within the inter-dendritic region, and the SC sensibility arises.[38,39]
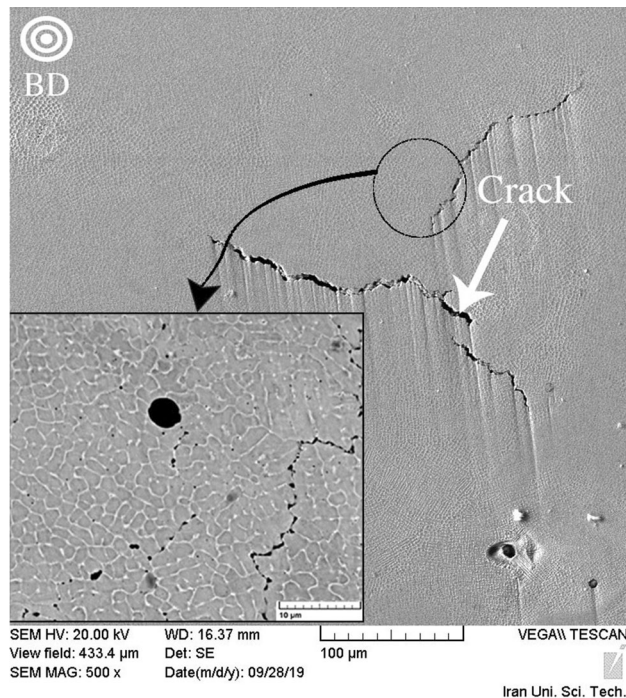
Concerning the effect of the VED on the cracking intensity, in low VEDs, very high cracking intensity was observed; meanwhile, with increasing VED, the probability of cracking occurrence decreased, as in the S8 specimen only a few cracks could be seen. The main reason for cracking in the as-built specimens is believed to be the SC mechanism, which can be eliminated through a lower cooling rate. As the VED increased, the input heat per volume increased obviously, which led to a lower cooling rate and lower susceptibility to SC. Figure 5 depicts the top surface of the S1, S5, and S8 specimens along with a graphical schematic of the cracking intensity.

After heat treatment, the issue of micro-cracking requires more attention. Our observations show that heat treatment promotes crack formation within the specimens. Figures 6(a) and (b) shows PWHT and DDC cracks on the top surface. The PWHT cracks were attributed to embrittlement of the grain boundaries, which contain brittle carbides, when the tensile stress was relaxed during heat treatment. The DDC crack occurred as a result of tensile stress relaxation during the heat treatment. The cracks were mainly directed along the grain boundaries, which is compatible with the findings of Marchese *et al.*[37] Figures 6(c) and (d), taken from the vertical (*i.e.*, X-Z) plane of the S5 specimen, shows the typical cracks produced in the heat-treated material where the carbides were concentrated. Thus, this issue may necessitate the application of a hot isostatic pressing (HIP) process as a part of the heat treatment process.

C. Microstructure Characterization

1. As-built material microstructure

Figures 7(a) through (c) shows SEM images of the produced morphology at the top surface (*i.e.*, perpendicular to the building direction) when low-, medium-, and high-range VEDs were applied. These images represent a periodic cellular dendritic microstructure pattern. The high solidification rate makes the heavy atoms such as Nb and Mo become entrapped in the inter-dendritic regions (see Figure 7(d)), which is called microsegregation. Zuback *et al.*[21] stated that microsegregation is directly attributed to the volume fraction of the Fe element. According to their study, a high fraction of Fe and a low fraction of Si (0.035 wt pct) elements lead to the formation of MN carbides, while no Laves phase is observed. According to the EDS results represented in Figures 7(d) and (e), the dendrite matrix is mainly composed of Ni and Cr, while high-intensity Nb and Mo elements are observed within the inter-dendritic regions.

Measuring 20 times on the top surface of each specimen showed that by increasing the VED from 108 to 156 J/mm^3, the inter-dendritic structure became thicker from 0.37 $\pm$ 0.05 to 0.83 $\pm$ 0.07 μm as a result of the lower cooling rate in high VEDs.[39,40] It is also important to point out that in low VEDs (*e.g.*, specimen S1), a partially formed inter-dendritic structure can be

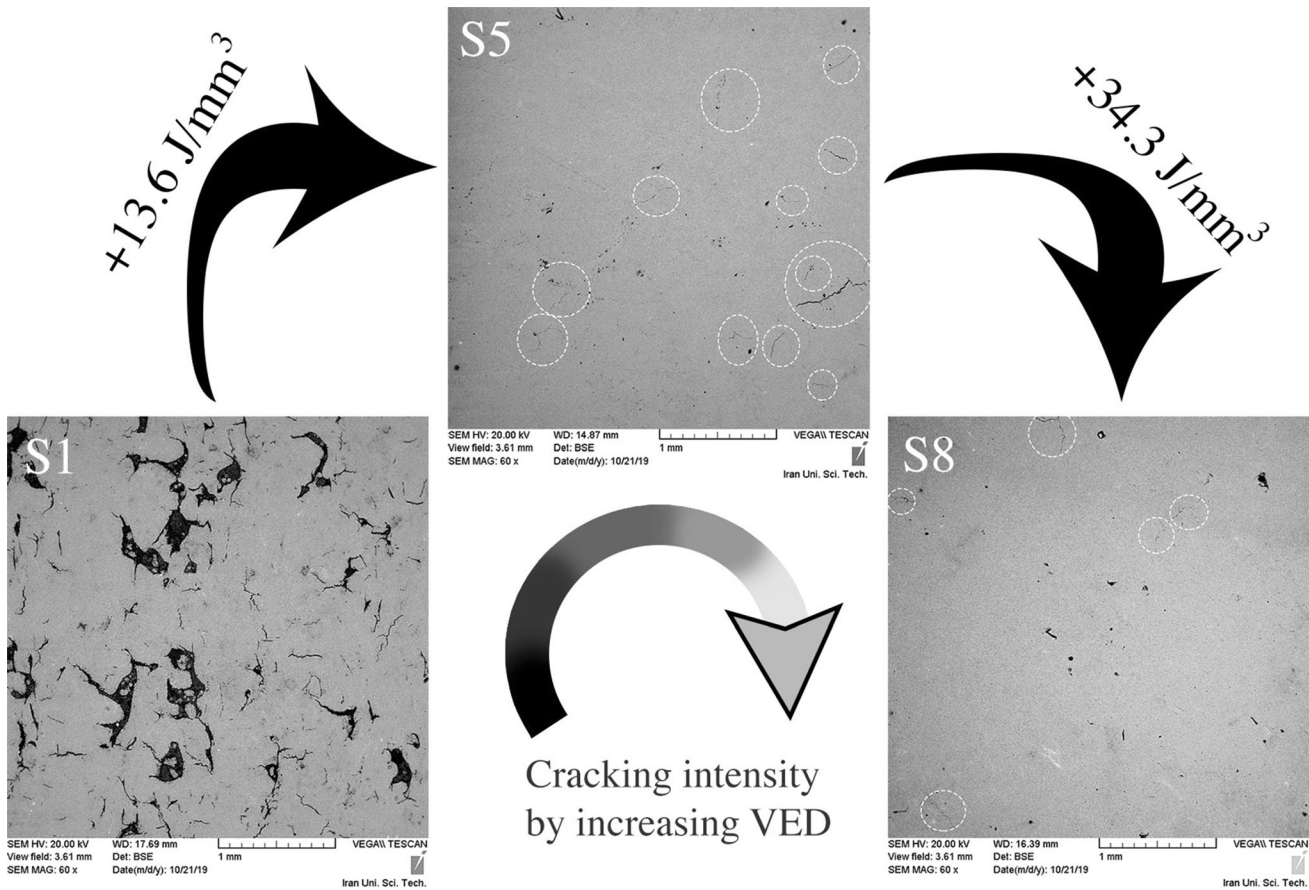Fig. 4—SEM image of inter-granular SC within the grain boundary.

Fig. 5—Cracking elimination through the increase of the VED; circles represent cracks.

seen because of the higher cooling rate. Thus, it is verified that by increasing the VED, and consequently decreasing the cooling rate, coarser cells are produced.

The layer-by-layer manufacturing process applies several heating cycles to the deposited material, which enables grain growth through the consecutive layers.[24] This matter results in columnar dendrites, which include cellular and elongated dendrites along the deposited layers.[7,25] It is reported that the last layers contain only cellular dendritic structures because of the lower number of the heating cycles and high cooling rate.[41,42] The high cooling rate can also result in different grain morphologies in a single melt pool (Figure 8(a)). Figures 8(b) and (c) shows the SEM images of the vertical plane (i.e., parallel to the build direction) of specimen S8, where the epitaxial growth of the dendritic microstructure occurred through the consecutive layers. It is obvious that the increase in the VED from 108 in S1 to 156 J/mm^3 in the S8 specimen caused longer dendrites. The direction of dendrite arms is fits well with the main heat flux direction during the manufacturing process. Amato et al.[43] pointed out this columnar microstructure is essentially parallel to the build direction; however, our observations indicate that the elongated dendrites are situated in different orientations. In fact, the direction of the heat flux is affected by the superposition result of the laser movement and heat conduction to the building platform. The width of the dendritic arms in a specific specimen is different because of the variation in the cooling rate at different sections.[39] We also know that DAS (λ) is directly related to the cooling rate (K/s) through the well-known equation $\lambda = K^{-0.33}$[8] in which K is a constant dependent on the material properties [i.e., 50 μm (K/s) for Ni-based alloys]. In the S8 specimen with 156 J/mm^3 VED, secondary dendrite arms (SDAs) are also observable because of the lower cooling rate, as shown in Figure 8(c).

As we expected from the used powder composition (Table I) and the previous works on the identification of the contributing phases of the as-built L-PBFed IN625,[10,26] only γ and γ'' phases exist within the microstructure and no Laves phase formed.

2. Heat-treated microstructure

In this study, specimens were subjected to solution annealing at 1100 °C for 1 hour and then aging post-processing at 700 °C for 8 hour. The two-step heat treatment was used for recrystallization and precipitation of hardening phases. As stated in the literature for SLMed IN625, the dendritic microstructure is stable up to 900 °C, and when the specimens were annealed at 1100 °C, equiaxed grains started to appear.[7] By considering the weight percentage of Fe (5.00 wt pct), Si (0.50 wt pct), and Ti (0.40 wt pct) and the temperature of Laves formation in the Zuback et al. work,[21] it is

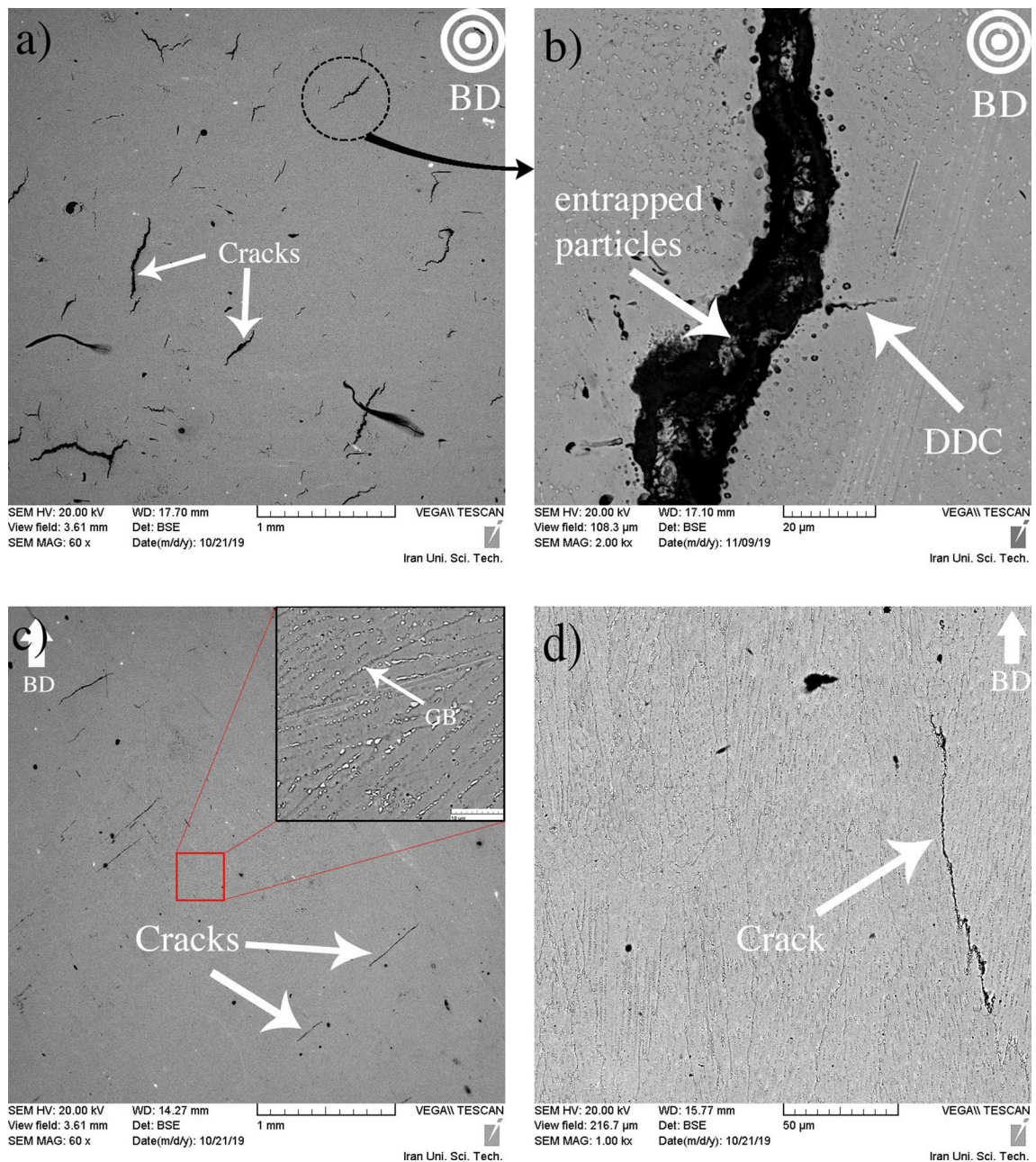Fig. 6—SEM images of large cracks in the horizontal and vertical planes of the specimens: (*a*) and (*b*) PWHT and DDC cracks in the heat-treated S4 specimen; (*c*) and (*d*) typical cracks produced in the heat-treated material (GB denotes the grain boundaries).

obvious that no Laves formed during annealing at 1100 °C. According to the T-T-T diagram of IN625,[30] aging at 700 °C for 8 hour eliminates the generation of Laves and δ phases. Furthermore, the benefit of aging is the precipitation of carbides within the grain boundaries and the formation of γ'' (Ni_3Nb), which strengthens the material.[26]

Figure 9 shows the microstructure of specimen S3 after the two-step heat treatment. It is observed that recrystallization took place with no evidence of a prior dendritic structure. The size of the recrystallized grain $\bar{a}$ was measured between 10 and 90 μm in the horizontal

plane, which was identical for all specimens. As included in Figure 9, EDS analysis of the precipitated phase indicates the presence of carbides. The carbide structure is rather hard and brittle and can cause cracks that can easily be broken at high temperatures.

Figure 10 depicts the microstructure of the vertical plane from specimen S6 before and after the two-step heat treatment and shows that very large grains were formed during the heat treatment. Although there is no evidence of the prior directional dendrites, segregated precipitates are mainly elongated parallel to the grain boundaries. We also detected Nb and Mo-rich
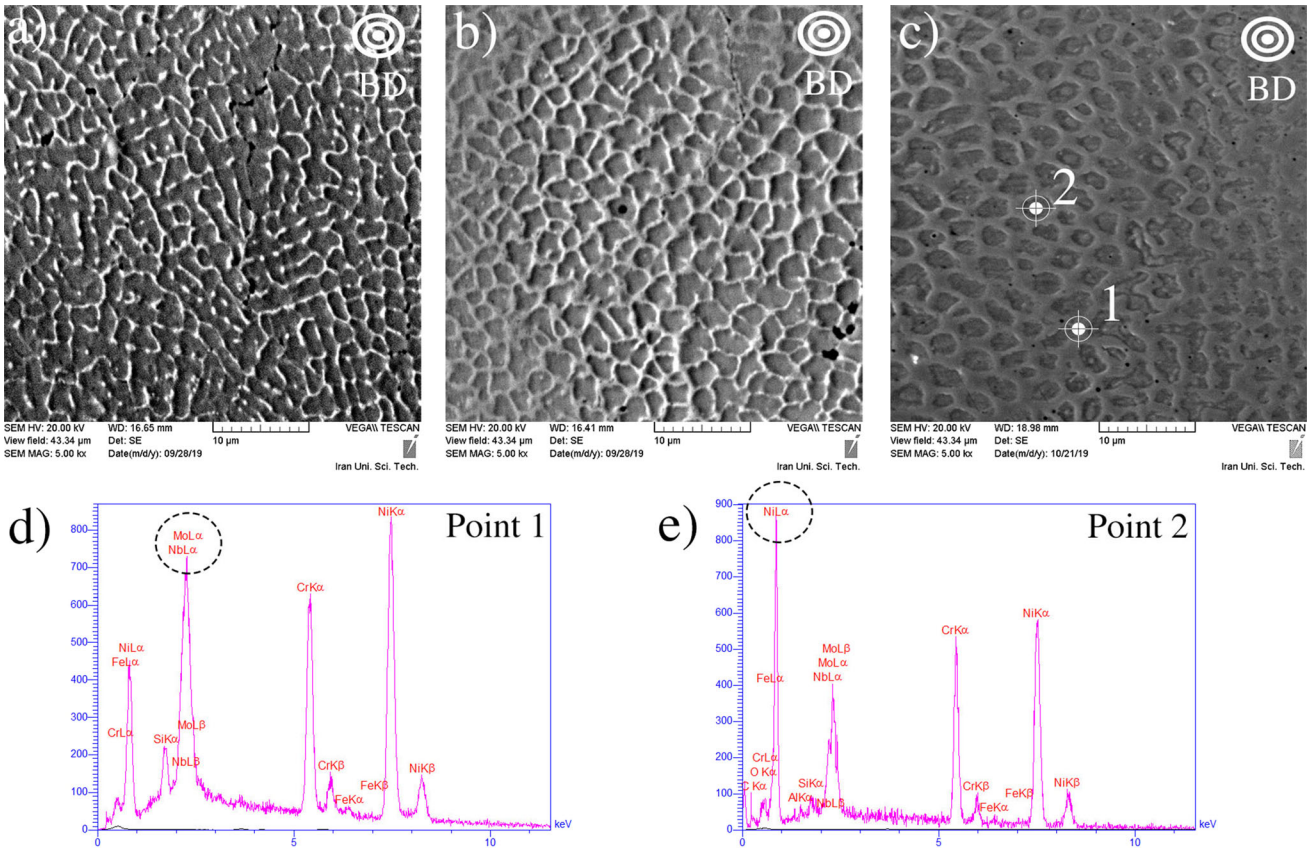
Fig. 7—SEM images of the produced morphology at the top surface. (*a*) Low-range VED; (*b*) medium-range VED; (*c*) high-range VED; (*d*) the EDS analysis of the target point from point 1; (*e*) the EDS analysis of the target point from point 2.
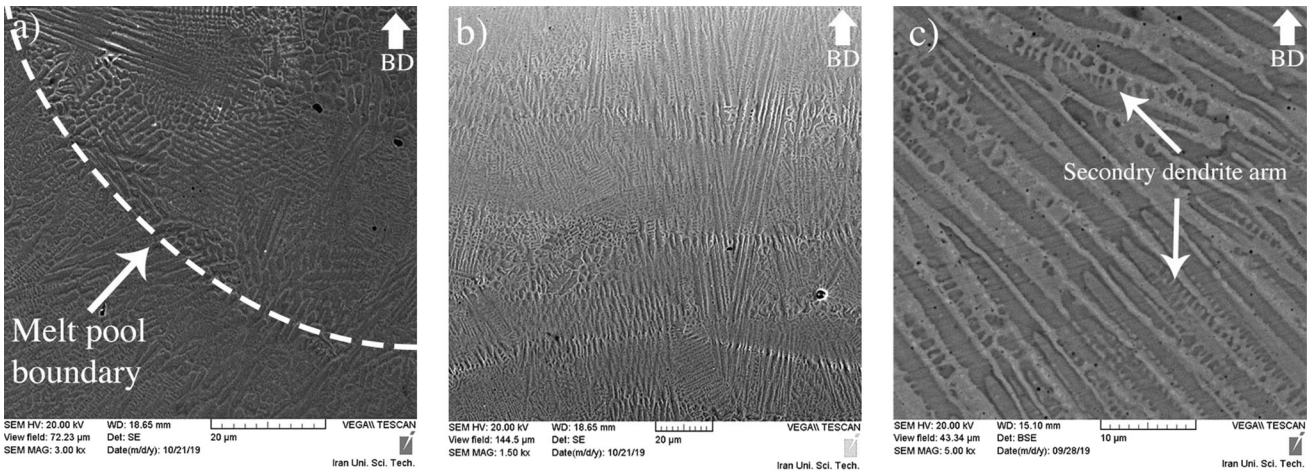

Fig. 8—SEM images of the vertical plane of specimen S8, representative of the elongated dendrite arms at different magnifications (*a*) ×3000; (*b*) ×1500; (*c*) ×5000.

precipitates; this may signify the presence of $MC/M_{23}C_6$ carbides that were mainly formed within the grain boundaries during the heat treatment (Figure 10). It is expected that γ'' phase is formed during the heat treatment, which cannot be detected using the available SEM because of its nanometric size.[12]

D. Hardness Measurements

Vickers hardness measurement was carried out on the top and side surfaces of both as-built and heat-treated specimens. Figure 11 shows the result of the hardness measurements. Due to the high cooling rate of the L-PBF process, heavy atoms such as Nb and Mo
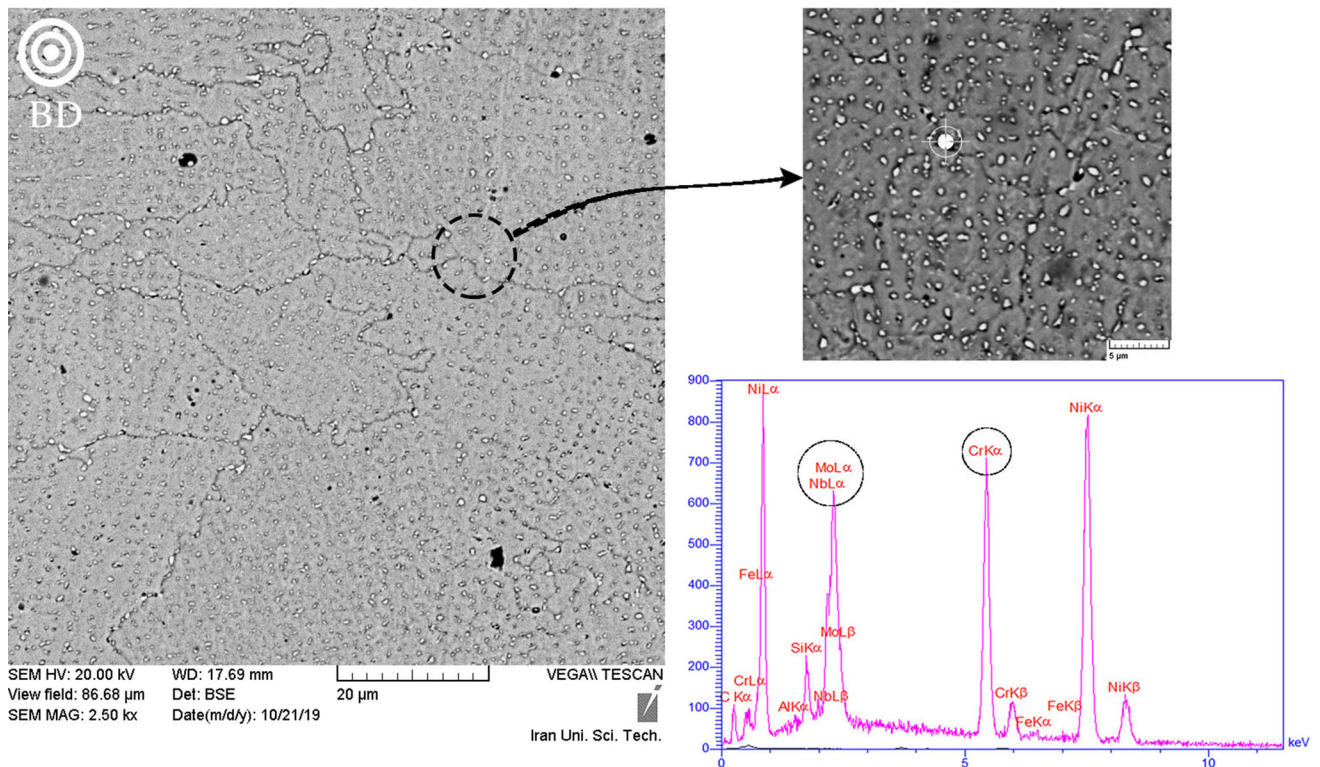
Fig. 9—SEM image of heat-treated grain morphology of specimen S3 along with the EDS analysis of the grain boundary.
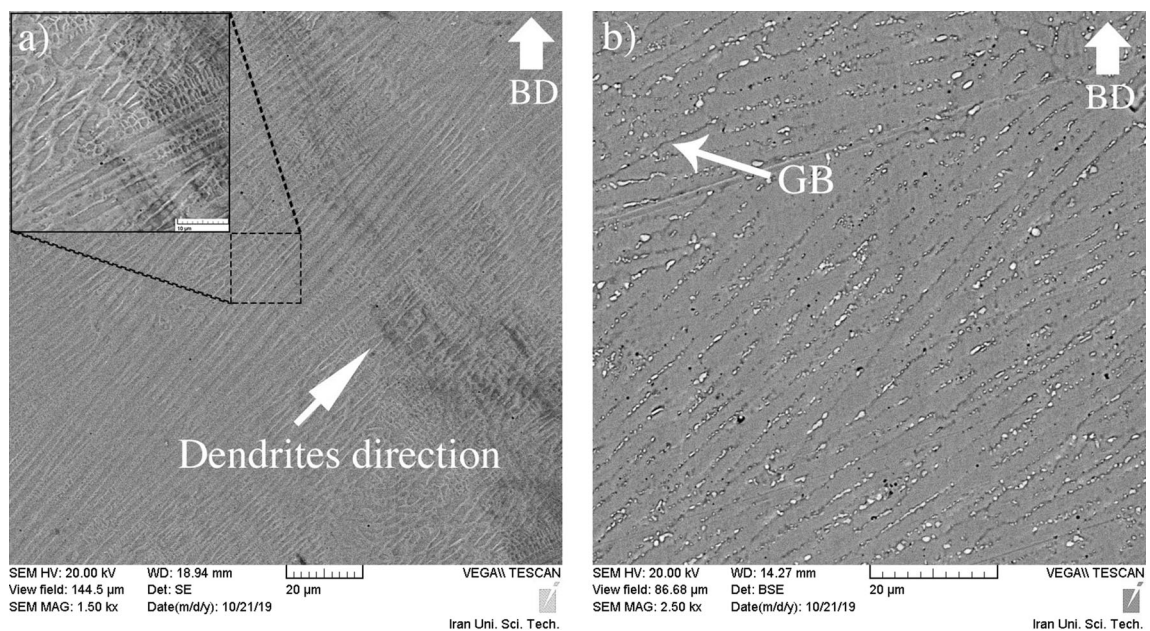

Fig. 10—SEM image of specimen S6 (*a*) before and (*b*) after heat treatment.

remained within the inter-dendritic structure, which acted as an obstacle against penetration of the indenter. This phenomenon causes higher hardness values to be measured for L-PBFed IN625 material compared with the wrought material (~ 305 HV for forged IN625).[8] According to the obtained results for the as-built specimens, the top surface hardness is higher than that of the relative side surface. It is seen that by increasing the VED, the top surface hardness in the as-built condition first increased from 292 to 344 HV and then decreased to about 320 HV. This obtained range for the hardness values on the top surface agrees fairly well with
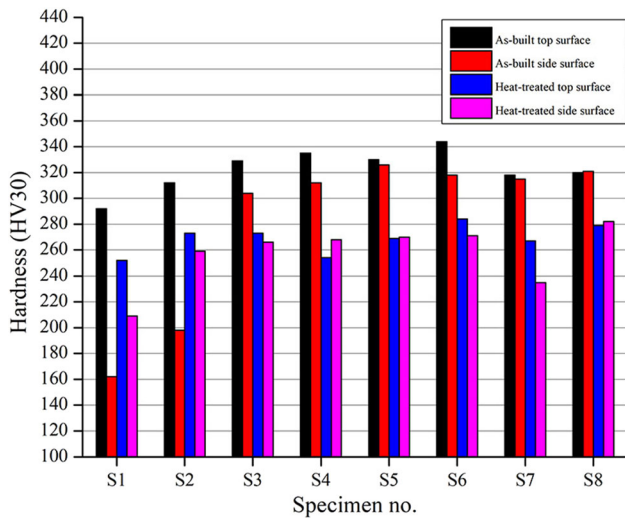
Fig. 11—Vickers hardness results on the top and side surfaces of the as-built and heat-treated specimens.

the previously reported values (290–320 HV).[11,44] The upward trend section is mainly because of the elimination of the porosity percentage. However, the downfall section can be explained through microstructural evolutions. According to the SEM images, as represented in Figure 7 for high-range VED, a lower cooling rate results in a smoother surface texture and coarser grains that lead to a lower hardness, as measured in the S7 and S8 specimens. Although the same trend is observed from the side surface hardness measurements, the measured hardness values were from 0.3 to 44 pct lower than those of the top surfaces. This difference tends to diminish with an increase in mass density; however, the effect of different morphologies remains.

In general, it is obvious that the heat-treated specimens show more homogeneous hardness properties than the as-built ones. The measured hardness values reveal that the solution-annealed specimens have lower hardness values on both sides, which is in agreement with References 7 and 10 The main reason for this argument is the formation of larger grains and residual stress relaxation during heat treatment.[10] Another reason for this reduction is related to the dissolution of the hardening phase during heat treatment. Marchese et al.[26] showed that after 2 hour of solution annealing at 1000 °C and 1150 °C, the hardness of the specimens was dramatically reduced as a result of recrystallization. However, it was shown that the 8-h aging process had a significant impact on hardness improvement after solution-annealing heat treatment.[26] Zhang et al.[45] proved that the volume fraction of precipitates increased as a result of expanding heat treatment duration up to 8 hour. As Marchese et al.[26] stated, the precipitated carbides (MC and/or $M_{23}C_6$) and formation of γ'' during the aging process are responsible for the hardness augmentation. Thus, the hardness of the specimens increased because of formation of hard precipitates during the aging process.

IV. CONCLUSIONS

In this article, we investigated the effect of the VED and heat treatment on the mass density, defect formation, microstructure, and hardness of IN625 manufactured by the L-PBF process. Eight sets of process parameters were implemented during the fabrication of specimens to provide a VED range between 108 and 156 J/mm^3. It is found that the VED has a direct effect on the mass density of the as-built specimens. In low VEDs, lack of fusion defects as well as solidification cracks is widely seen, while in high VEDs keyhole defects are prominent. Gas pores are always present, but their size and population depend on the applied VED. Specimens fabricated with high VEDs are less susceptible to cracking occurrence. Micro-crack formation is also dependent on the heat treatment through a mechanism called post-weld heat treatment. An increase in the VED causes longer and coarser dendrites. The microstructural analysis after the heat treatment showed several precipitates, while fine dendrites disappeared. The hardness of the as-built specimens showed a variation that mainly contributed to the porosity percentage of the specimens and obviously the applied VED. The hardness of the heat-treated specimens first rose sharply with increasing VED and then reached a plateau. However, when heat treatment was applied, the hardness tended to decrease with a lower variation between the top and side surfaces of each specimen.

DATA AVAILABILITY

Most of the raw/processed data required to reproduce these findings have been given in the text. However, any additional data can be shared upon request.

REFERENCES

1. C. Weller, R. Kleer, and F.T. Piller: *Int. J. Prod. Econ.*, 2015, vol. 164, pp. 43–56, https://doi.org/10.1016/j.ijpe.2015.02.020.
2. S. Ford and M. Despeisse: *J. Clean. Prod.*, 2016, vol. 137, pp. 1573–87, https://doi.org/10.1016/j.jclepro.2016.04.150.
3. A. Sola and A. Nouri: *J. Adv. Manuf. Process.*, 2019, vol. 1 (3), pp. 1–21, https://doi.org/10.1002/amp2.10021.
4. J.A. Gonzalez, J. Mireles, S.W. Stafford, M.A. Perez, C.A. Terrazas, and R.B. Wicker: *J. Mater. Process. Tech.*, 2019, vol. 264, pp. 200–10, https://doi.org/10.1016/j.jmatprotec.2018.08.031.
5. V.A. Popovich, E.V. Borisov, A.A. Popovich, V.S. Sufiiarov, D.V. Masaylo, and L. Alzina: *Mater. Des.*, 2017, vol. 131, pp. 12–22, https://doi.org/10.1016/j.matdes.2017.05.065.
6. B. Dubiel and J. Sieniawski: *Materials*, 2019, vol. 12, p. 1144, https://doi.org/10.3390/ma12071144.
7. J. Nguejio, F.. Szmytka, S. Hallais, A. Tanguy, S. Nardone, and M. Godino Martinez: *Mater. Sci. Eng. A*, 2019, vol. 764, p. 138214, https://doi.org/10.1016/j.msea.2019.138214.
8. S. Li, Q. Wei, Y. Shi, Z. Zhu, and D. Zhang: *J. Mater. Sci. Tech.*, 2015, vol. 31 (9), pp. 946–52, https://doi.org/10.1016/j.jmst.2014.09.020.
9. I.A. Choudhury and M.A. El-Baradie: *J. Mater. Proc. Tech.*, 1998, vol. 77 (1–3), pp. 278–84, https://doi.org/10.1016/S0924-0136(97)00429-9.

10. C. Li, R. White, X.Y. Fang, M. Weaver, and Y.B. Guo: *Mater. Sci. Eng. A*, 2017, vol. 705, pp. 20–31, https://doi.org/10.1016/j.msea.2017.08.058.
11. P. Liu, S. Sun, M. Cao, J. Gong, and J. Hu: *High. Temp. Mater. Process.*, 2019, vol. 38, pp. 229–36, https://doi.org/10.1515/htmp-2017-0182.
12. Z. Wang, K. Guan, M. Gao, X. Li, X. Chen, and X. Zeng: *J. Alloy. Compd.*, 2012, vol. 513, pp. 518–23, https://doi.org/10.1016/j.jallcom.2011.10.107.
13. N.H. Sateesh, G.C. Mohan Kumar, K. Prasad, C.K. Srinivas, and A.R. Vinod: *Process. Mater. Sci.*, 2014, vol. 5, pp. 772–79, https://doi.org/10.1016/j.mspro.2014.07.327.
14. L.N. Carter, X. Wang, N. Read, R. Khan, M. Aristizabal, K. Essa, and M.M. Attallah: *Mater. Sci. Tech.*, 2016, vol. 32 (7), pp. 657–61, https://doi.org/10.1179/1743284715Y.0000000108.
15. M. Amirjan and H. Sakiani: *Int. J. Adv. Manuf. Technol.*, 2019, vol. 103, pp. 1769–80, https://doi.org/10.1007/s00170-019-03545-0.
16. I. Koutiri, E. Pessard, P. Peyre, O. Amlou, and T. De Terrisa: *J. Mater. Process. Tech.*, 2018, vol. 255, pp. 536–46, https://doi.org/10.1016/j.jmatprotec.2017.12.043.
17. L.E. Criales, Y.M. Arısoy, B. Lane, S. Moylan, A. Donmez, and T. Özel: *Int. J. Mach. Tool. Manuf.*, 2017, vol. 121, pp. 22–36, https://doi.org/10.1016/j.ijmachtools.2017.03.004.
18. M.A. Anam, D. Pal and B. Stucker: *Proceeding of the 24th Annual International Solid Free form Fabrication Symposium-An Additive Manufacturing Conference*, Austin, TX, 2013, pp. 463–73. https://doi.org/10.13140/2.1.4009.1201.
19. K. Moussaoui, W. Rubio, M. Mousseigne, T. Sultan, and F. Rezai: *Mater. Sci. Eng. A*, 2018, vol. 735, pp. 182–90, https://doi.org/10.1016/j.msea.2018.08.037.
20. D. Zhang, W.. Niu, X. Cao, and Z. Liu: *Mater. Sci. Eng. A*, 2015, vol. 644, pp. 32–40, https://doi.org/10.1016/j.msea.2015.06.021.
21. J.S. Zuback, P. Moradifar, Z. Khayat, N. Alem, and T.A. Palmer: *J. Alloy. Compd.*, 2019, vol. 798, pp. 446–57, https://doi.org/10.1016/j.jallcom.2019.05.230.
22. C.C. Silva, H.C. de Miranda, M.F. Motta, J.P. Farias, C.R.M. Afonso, and A.J. Ramirez: *J. Mater. Res. Technol.*, 2013, vol. 2 (3), pp. 228–37, https://doi.org/10.1016/j.jmrt.2013.02.008.
23. S.J. Foster, K. Carver, R.B. Dinwiddie, F. List, III, K.A. Unocic, A. Chaudhary, and S.S. Babu: *Metal. Mater. Trans. A*, 2018, vol. 49A, pp. 5775–98, https://doi.org/10.1007/s11661-018-4870-2.
24. A. Kreitcberg, V. Brailovski, and S. Turenne: *Mater. Sci. Eng. A*, 2017, vol. 689, pp. 1–10, https://doi.org/10.1016/j.msea.2017.02.038.
25. S. Raghavan, B. Zhang, P. Wang, C.-N. Sun, M.L. Sharon Nai, T. Li, and J. Wei: *Mater. Manuf. Process.*, 2017, vol. 32 (14), pp. 1588–95, https://doi.org/10.1080/10426914.2016.1257805.
26. G. Marchese, M. Lorusso, S. Parizia, E. Bassini, J.-W. Lee, F.. Calignano, D. Manfredi, M. Terner, H.-U. Hong, D. Ugues, M. Lombardi, and S. Biamino: *Mater. Sci. Eng. A*, 2018, vol. 729, pp. 64–75, https://doi.org/10.1016/j.msea.2018.05.044.
27. E.A. Lass, M.R. Stoudt, M.B. Katz, and M.E. Williams: *Scripta. Mater.*, 2018, vol. 154, pp. 83–86, https://doi.org/10.1016/j.scriptamat.2018.05.025.
28. A. El Hassanin, F. Scherillo, A.T. Silvestri, A. Caraviello, R. Sansone, A. Astarita, and A. Squillace: *AIP Conf. Proc.*, 2019, vol. 2113, p. 060004, https://doi.org/10.1063/1.5112599.
29. EOS Nickel Alloy IN625 Material Data Sheet. Electro Optical Systems. https://dmlstechnology.com/images/pdf/EOS_NickelAlloy_IN625.pdf.
30. I.J. Moore, J.I. Taylor, M.W. Tracy, M.G. Burke, and E.J. Palmiere: *Mater. Sci. Eng. A*, 2017, vol. 682, pp. 402–09, https://doi.org/10.1016/j.msea.2016.11.060.
31. H.R. Javidrad and S. Salemi: *Int. J. Adv. Manuf. Technol.*, 2020, vol. 107, pp. 4597–4607, https://doi.org/10.1007/s00170-020-05321-x.
32. C. Pleass and S. Jothi: *Addit. Manuf.*, 2018, vol. 24, pp. 419–31, https://doi.org/10.1016/j.addma.2018.09.023.
33. M.M. Attallah, R. Jennings, X. Wang, and L.N. Carter: *MRS Bull.*, 2016, vol. 41 (10), pp. 758–64, https://doi.org/10.1557/mrs.2016.211.
34. H. Kim and S.P. Moylan: *Adv. Manuf. Ser.*, 2018, vol. 100, p. 16, https://doi.org/10.6028/NIST.AMS.100-16.
35. H.-Y. Wan, Z.-J. Zhou, C.-P. Li, G.-F. Chen, and G.-P. Zhang: *Adv. Eng. Mater.*, 2018, vol. 20 (10), p. 1800307, https://doi.org/10.1002/adem.201800307.
36. X. Zhang, H. Chen, L. Xu, J. Xu, X. Ren, and X. Chen: *Mater. Des.*, 2019, vol. 183, p. 108105, https://doi.org/10.1016/j.matdes.2019.108105.
37. G. Marchese, G. Basile, E. Bassini, A. Aversa, M. Lombardi, D. Ugues, P. Fino, and S. Biamino: *Materials*, 2018, vol. 11, p. 106, https://doi.org/10.3390/ma11010106.
38. H. Xiao, S.M. Li, W.J. Xiao, Y.Q. Li, L.M. Cha, J. Mazumder, and L.J. Song: *Mater. Lett.*, 2017, vol. 188, pp. 260–62, https://doi.org/10.1016/j.matlet.2016.10.118.
39. A.P.R. Mostafa, V. Brailovski, M. Jahazi, and M. Medraj: *Metals*, 2017, vol. 7 (6), p. 196, https://doi.org/10.3390/met7060196.
40. C. Li, Y.B. Guo, and J.B. Zhao: *J. Mater. Process. Tech.*, 2017, vol. 243, pp. 269–81, https://doi.org/10.1016/j.jmatprotec.2016.12.033.
41. S. Cao, D. Gu, and Q. Shi: *J. Alloy. Compd.*, 2017, vol. 692, pp. 758–69, https://doi.org/10.1016/j.jallcom.2016.09.098.
42. M. Cabrini, S. Lorenzi, C. Testa, F. Brevi, S. Biamino, P. Fino, D. Manfredi, G. Marchese, F. Calignano, and T. Pastore: *Materials*, 2019, vol. 12, p. 1742, https://doi.org/10.3390/ma12111742.
43. K.N. Amato, S.M. Gaytan, L.E. Murr, E. Martinez, P.W. Shindo, J. Hernandez, S. Collins, and F. Medina: *Acta. Mater.*, 2012, vol. 60 (5), pp. 2229–39, https://doi.org/10.1016/j.actamat.2011.12.032.
44. G. Marchese, X.G. Colera, F. Calignano, M. Lorusso, S. Biamino, P. Minetola, and D. Manfredi: *Adv. Eng. Mater.*, 2016, https://doi.org/10.1002/adem.201600635.
45. F. Zhang, L.E. Levine, A.J. Allen, M.R. Stoudt, G. Lindwall, E.A. Lass, M.E. Williams, Y. Idell, and C.E. Campbell: *Acta. Mater.*, 2018, vol. 152, pp. 200–14, https://doi.org/10.1016/j.actamat.2018.03.017.

Publisher's Note Springer Nature remains neutral with regard to jurisdictional claims in published maps and institutional affiliations.